

A Theoretical Stereoselectivity Model of Photochemical Denitrogenations of Diazoalkanes Towards Strained 1,3-Dihalogenated Bicyclobutanes

Jingbai Li, Rachel Stein, and Steven A. Lopez*

Department of Chemistry & Chemical Biology, Northeastern University, 360 Huntington Ave, Boston MA, 02115

Abstract

Photochemical reactions exemplify ‘green’ chemistry and are essential for synthesizing highly strained molecules with mild conditions with light. The light-promoted denitrogenation of bicyclic azoalkanes affords functionalized, stereo-enriched bicyclo[1.1.0]butanes. We revisited these reactions with multireference calculations and non-adiabatic molecular dynamics (NAMD) simulations for a series of diazabicyclo[2.1.1]hexenes to predict the photophysics, reactivities, and stereoselectivities. We used complete active space self-consistent field (CASSCF) calculations with an (8,8) active space and ANO-S-VDZP basis set; the CASSCF energies were corrected with CASPT2(8,8)/ANO-S-VDZP. The excitation is consistently $n \rightarrow \pi^*$ and ranges from 3.77–3.91 eV for the diazabicyclo[2.1.1]hexenes. Minimum energy path calculations showed stepwise C–N bond breaking and led to a minimum energy crossing point, which favors the stereochemical ‘double inversion’ bicyclobutane product. Wigner sampling of **1** provided Franck-Condon points for 692 NAMD trajectories. We identified competing complete stereoselective and stereochemical scrambling pathways. The stereoselective pathways feature concerted bicyclobutane inversion and N_2 extrusion. The stereochemical scrambling pathways involve N_2 extrusion followed by bicyclobutane planarization, leading to non-stereoselective outcomes. The predicted diastereomeric excess almost exactly match experiment (calc.d.e.=46% vs. exp.d.e.=47%). Our NAMD simulations with 672, 568, and 596 trajectories for **1-F**, **1-Cl**, and **1-Br** predicted diastereomeric excess (d.e.) of 94–97% for the double inversion products. Halogenation significantly perturbs the potential energy surface (PES) towards the retention products because of powerful hyperconjugative interactions. The $n_C \rightarrow \sigma^*_{C-X}$, $X = F, Cl, Br$ hyperconjugative interaction leads to a broadened shoulder region on the PES for double inversion.

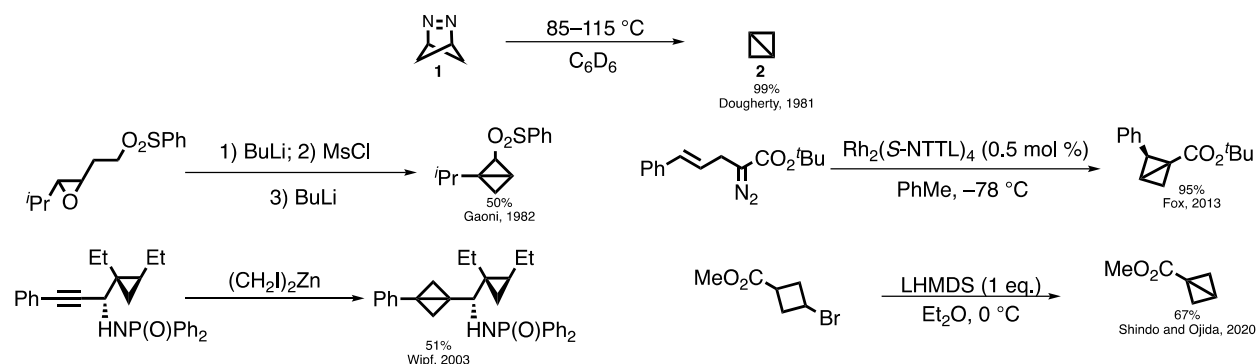
Introduction

Photochemical transformations offer efficient access to highly strained molecular architectures with mild reaction conditions and a light source. Photochemistry falls under the umbrella of *green* chemistry because it does not require rare-earth organometallic catalysts or extended periods of reaction heating to achieve the same reaction outcome. The light-promoted denitrogenation is one of the cleanest and most convenient reactions because the byproduct is nitrogen gas. One important and underexplored reaction is the denitrogenation of cyclic azoalkanes, for instance diazabicyclo[2.1.1]hex-2-ene (**1**) to afford bicyclo[1.1.0]butane (**2**) under thermal conditions.¹

Bicyclo[1.1.0]butane is the most strained carbon-based bi-cycle with the strain energy approaching 66 kcal mol⁻¹.² The central σ_{C-C} bond bends the plane of two cyclopropane exposing the *p*-orbitals that are ready for nucleophilic³⁻⁴ and electrophilic⁴ reactions. These properties give

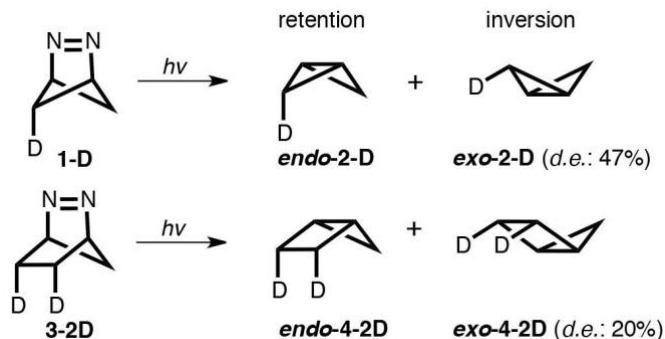
bicyclo[1.1.0]butane a great potential in broad applications.⁵⁻⁷ The strained structure of bicyclo[1.1.0]butane makes the synthesis and functionalization rather challenging. The current functionalization can only access the bridge-head carbons. Thus, the chemical potential of bicyclo[1.1.0]butane has not been fully exploited. Scheme 1 summarizes synthetic routines to prepare bicyclo[1.1.0]butane and the derivatives.⁸⁻¹²

Scheme 1. Synthesis of bicyclo[1.1.0]butane.



The decomposition of cyclic azoalkanes toward carbon-based bi-cycles has been extensively studied by thermolysis^{8, 13-15} and photolysis¹⁶ in solution⁸, gas phase¹³, or solid-state.¹⁷ Dougherty and co-workers have investigated the deuterated diazabicyclo[2.1.1]hex-2-ene (**1-D**). They measured a 47% excess of **exo-2-D** in the singlet state photolysis¹⁶ (Scheme 2), while the thermolysis of **1-D** led to stereorandom products due to possible formation of symmetric cyclobutane diradical intermediate.¹³ Later, Roth and co-workers have discovered a diastereoselective denitrogenation mechanism of irradiating diazabicyclo[2.2.1]hept-2-ene (**3**) and discovered a 20% diastereomeric excess of the inverted product **exo-4-2D**¹⁸ (Scheme 2). Trofimov and co-workers confirmed the inversion is all preferred in several derivatives of **3**.¹⁹ Adam and co-workers performed a photochemical reaction involving a photosensitizer (triplet benzene), but observed no diastereomeric excess as forming the cyclopentane diradical intermediate.²⁰

Scheme 2. Diastereoselectivity in the direct photolysis of cyclic azoalkanes.

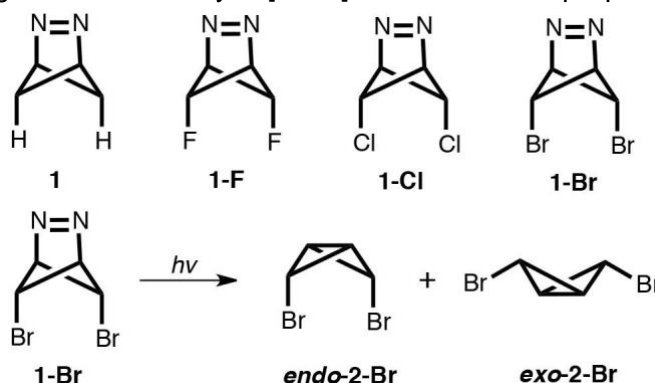


Quantum mechanical calculations have provided detailed insights to the photochemical stereoselectivities of **1** and **3**. In 1998, Olivucci and Robb located and characterized a diazenyl

diradical conical intersection of **3** with complete active space self-consistent field (10 electron and 8 orbitals) and 6-31G^{*} basis set, which suggested a preferential path to inversion mechanism.²¹ In 2003, Olivucci and co-workers published a single classical trajectory with B3LYP functional and 6-31G^{*} basis set to probe the reaction path from their previously located diazenyl diradical conical intersection. They concluded that the stereoselectivity was attributed to an impulsively populated inversion vibrational mode.²² Li and co-workers then located a diazenyl diradical conical intersection of **1** with a 12 electron and 10 orbitals active space and 6-311G^{**} basis set in 2006; the minimum energy path proceeded to the double-inversion product.²³ Most recently, Abe and co-workers reviewed that the interplay between diazenyl and 1,3-diyl diradicals is responsible for the stereoselectivity during the denitrogenation of cyclic azoalkanes.²⁴ However, all theoretical works were limited to qualitative rationale for the stereoselectivity, thus have not fully explained the measured diastereomeric excess.

We revisited photophysics and photochemistry of **1** with multiconfigurational calculations and used non-adiabatic molecular dynamics simulations to quantify the stereoselectivity. The dynamics simulations uncovered the mechanistic origin of the stereoselectivity in the denitrogenation of **1**. We applied our dynamics model to predict the stereoselectivities of a series of 1,3-dihalogenated diazabicyclo[2.1.1]hexa-2-enes, as shown in Scheme 3 (**1-F**, **1-Cl**, **1-Br**). In particular, we are interested in 1,3-dibromo diazabicyclo[2.1.1]hexa-2-ene (**1-Br**), because it enables the access to the cyclic carbon in the bicyclo[1.1.0]butane derivative (**2-Br**) for subsequent fluorination, chlorination, and alkylation reactions towards value-added molecules and materials. Our computations focus on uncovering the effect of halogenation on the denitrogenation stereoselectivities.

Scheme 3. 1,3-dihalogenated diazabicyclo[2.1.1]hexa-2-ene and proposed denitrogenation.



Computational Methods

Multiconfigurational calculations. Our multiconfigurational calculations employed the state-averaged CASSCF with single-state CASPT2 corrections, implemented in OpenMolcas 19.11.²⁶ In previous study on the unsubstituted **1** and **3**, Li²³ and Olivucci²² have constructed an active space consisting of 12 electrons and 10 orbitals (*i.e.*, (12,10)), featuring 4 electrons from the $\sigma_{\text{N=N}}/\sigma_{\text{N=N}}^*$ and $\pi_{\text{N=N}}/\pi_{\text{N=N}}^*$ orbitals, 4 electrons from two lone pair orbitals ($n_{\text{N=N}}$) of endocyclic nitrogens, and 4 electrons from two sets of $\sigma_{\text{C-N}}/\sigma_{\text{C-N}}^*$ orbitals. We chose an active space of 8

electrons and 8 orbitals because the nitrogen lone pair orbitals become less active during state averaging in the reactant with the occupations near 2.00. In the (8,8) active space, the second $\sigma_{\text{C-N}}$ orbital is notably localized on nitrogen atoms showing non-bonding character, consistent with a previous time-dependent density functional theory study by Ciofini and co-workers.²⁷ As we will discuss in the photophysics section, the (8,8) space reproduced the excitation energy corresponding to the experimental absorption spectrum. The (8,8) active space requires substantially reduced computational cost relative to the (12,10) space. As such, we chose it for our state averaged CASSCF calculations. Figure 1 illustrates the orbitals and average occupancies of our selected (8,8) active space in **1-Br**.

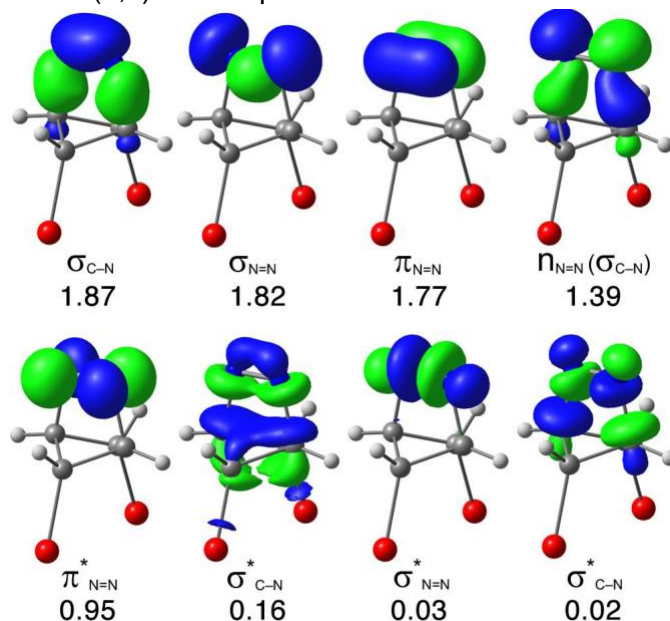


Figure 1. The (8,8) active space of **1-Br**. The occupation numbers are averaged over 7 states, computed at CASSCF(8,8)/ANO-S-VDZP. Isosurface value = 0.08. The active spaces for **1**, **1-F**, and **1-Cl** are available in Supporting Information.

The optimized geometries with the (8,8) space used ANO-S-VDZP basis set.²⁸⁻³¹ Subsequent vibrational analysis confirmed that ground-state geometry, **S₀-1**, **S₀-1-F**, **S₀-1-Cl**, and **S₀-1-Br** were indeed local minima with all positive frequencies. We performed a minimum energy path (MEP) calculations from the S₁-Franck-Condon point. We optimized S₁/S₀ minimum energy crossing points (**MECP-1**, **MECP-1-F**, **MECP-1-Cl** and **MECP-1-Br**) with CASSCF(8,8)/ANO-S-VDZP. The CASPT2(8,8) corrections to the electronic energy included a shift of 0.3 Hartree to avoid intruder states.³²⁻³³

We established four reaction coordinates (R1, R2, α , and θ) to track the geometries of **1** and **1-Br**, along the ground- and excited-states. R1 represents the length of the first breaking C–N bond and R2 is the length of the second breaking C–N bond. We defined an angle θ to determine the bicyclobutane dihedral between the cyclopropyl rings. We introduced the hydrogen dihedral angle α to describe the relative position of the hydrogen atom on the bond-breaking carbon atom with respect to the cyclopropyl plane. Figure 2 shows the distance R1 and R2 and dihedral angle θ and α in **S₀-1-Br** and **MECP-1-Br**.

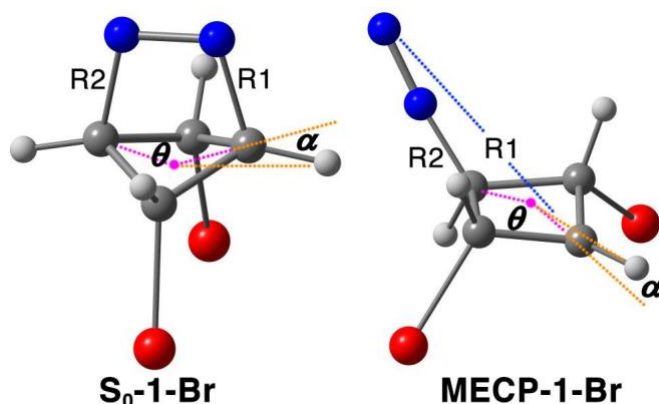


Figure 2. The CASSCF(8,8)/ANO-S-VDZP optimized geometries of **S₀-1-Br** and **MECP-1-Br**. The pink dotted lines highlight the bicyclobutane dihedral angle θ between the cyclopropyl rings. The θ in $-180-0^\circ$ was converted in $180-360^\circ$. The yellow dotted lines show the hydrogen dihedral angle α between the cyclopropyl plane and the hydrogen atom sharing the same edge of θ . $\alpha > 0$, when the hydrogen atom is above the cyclopropyl plane; $\alpha < 0$, when the hydrogen atom is under the cyclopropyl plane. The blue dotted line indicated the R1 distance in the broken C–N bond. In **S₀-1-Br**, $R1 = R2 = 1.56\text{\AA}$, $\theta = 136^\circ$, and $\alpha = -17^\circ$; in **MECP-1-Br**, $R1 = 4.35\text{\AA}$, $R2 = 1.41\text{\AA}$, $\theta = 197^\circ$, and $\alpha = 5^\circ$. The optimized geometries for **1**, **1-F**, and **1-Cl** are available in the Supporting Information.

Potential energy surface scans. We computed potential energy surfaces (PESs) for **1**, **1-F**, **1-Cl**, and **1-Br** with CASSCF(8,8)/ANO-S-VDZP by scanning the bicyclobutane dihedral angle, θ from 160° to 200° and the hydrogen dihedral angle α from -20° to 20° with a 4° step size for θ and α . We constrained one of C–N bond to 1.48\AA to prevent the dissociation of N_2 in **1-F**, **1-Cl**, **1-Br**, which often led to unconverged geometries. The PESs of **1** are nearly identical with and without the C–N bond constraint. We also computed PESs for **2**, **2-F**, **2-Cl**, and **2-Br** with CASSCF(2,2)/ANO-S-VDZP by removing nitrogen atoms and corresponding active orbitals. The scan of the hydrogen dihedral angle α constrained both bridge-head hydrogen atoms and varied them simultaneously.

Non-adiabatic molecular dynamics. Non-adiabatic molecular dynamics (NAMD) simulation classically propagates the nuclear positions on potential energy surfaces obtained from multiconfigurational electronic calculation. We sampled the initial conditions (nuclear positions and velocities) from the vibrational modes in Wigner distribution at 300 K. The electronic calculations used CASSCF(8,8)/ANO-S-VDZP. The trajectories started from the S_1 Franck-Condon point and the simulation time was 300 fs with a 0.5 fs time step. We applied the Nosé-Hoover thermostat³⁴ to equilibrate the ensemble temperature at 300K. The surface hopping probability was computed with Tully’s fewest switches surface hopping method³⁵⁻³⁷ implemented in OpenMolcas.²⁶

Natural bond orbital analysis. We quantified the carbon–halogen bond hyperconjugations in the transition state between the retention and inversion products using the natural bond orbital (NBO) analysis³⁸ implemented in GenNBO6.0.³⁹ The orbital interactions were computed using second order perturbation of Fock matrix in NBO basis (*i.e.*, $E^{(2)}$ energy).³⁸ The $E^{(2)}$ energy is defined as $E^{(2)} = F_{d,a}^2 / \Delta E_{d,a}$, where $F_{d,a}$ is the one-electron integral over donor and acceptor orbitals and $\Delta E_{d,a}$ is the orbital energy difference. The $E^{(2)}$ energy is positive meaning the magnitude of

the energetic stabilization gained from orbital interactions. The single point calculations employed PBE0⁴⁰⁻⁴¹ density functional and cc-pVDZ⁴² basis set available in ORCA 4.2.0.⁴³ We used the broken-symmetry formalism⁴⁴ of density functional theory to properly address the multiconfigurational characters in the transition state structures.

Results and Discussion

Photo-excitation of 1 and 1-Br. The electronic excitation of **1** is a well-known $n \rightarrow \pi^*$ transition; this corresponds to an excitation of an electron from a diazo nitrogen lone pair orbital (n) to its $\pi^*_{N=N}$ -orbital. We have computed the photophysical properties to validate the (8,8) active space for **1** and its halogenated derivatives. Table 1 shows the computed S_1 excitation energies, electronic transitions, and oscillator strengths.

Table 1. Vertical excitation energies, electronic transitions, and oscillator strengths of **1** and **1-X** ($X = F, Cl, Br$) with CASPT2(8,8)/ANO-S-VDZP//CASSCF(8,8)/ANO-S-VDZP.

Compounds	S_1 Energy (eV)	Transition	Oscillator strength
1	3.91	$n \rightarrow \pi^*$	$1.13 \cdot 10^{-2}$
1-F	3.79	$n \rightarrow \pi^*$	$8.53 \cdot 10^{-3}$
1-Cl	3.78	$n \rightarrow \pi^*$	$6.80 \cdot 10^{-3}$
1-Br	3.77	$n \rightarrow \pi^*$	$6.26 \cdot 10^{-3}$

^aOscillator strengths are computed with CASSCF(8,8)/ANO-S-VDZP.

The CASPT2(8,8)/ANO-S-VDZP//CASSCF(8,8)/ANO-S-VDZP calculation of **1** predicted an S_1 state with $n\pi^*$ character. The excitation energy was 3.91 eV, which agrees with the experimental absorbance $\lambda_{\max} = 330$ nm (3.75 eV).⁸ The oscillator strength for this transition is $1.13 \cdot 10^{-2}$. The halogenated reactants (**1-F**, **1-Cl**, and **1-Br**) have lower excitation energies (3.77–3.79 eV, respectively) and lower oscillator strengths (8.53 – $6.26 \cdot 10^{-3}$). The decreasing oscillator strength suggests the halogen atoms may result in a lower quantum yield for these reactants due to less efficient $n \rightarrow \pi^*$ excitations. Our CASSCF(8,8)/ANO-S-VDZP calculations overestimated the excitation energies because of the missing electronic dynamic correlations (Table S1). The CASSCF(8,8)/ANO-S-VDZP calculations predicted an consistent $n \rightarrow \pi^*$ transition, thus is qualitatively reliable to study the photochemistry of **1** and **1-Br** from the S_1 Franck-Condon points.

We computed the minimum energy path (MEP) to explore the steepest descent path from **S₁-FC-1** and **S₁-FC-1-Br**. The MEP from **S₁-FC-1** has been previously reported by Li and co-workers.²³ Our new calculations on **1-F** and **1-Cl** showed similar MEP to the parent **1** (Figure S3), while **1-Br** offers a substantially different MEP starting from **S₁-FC-1-Br** (Figure 3).

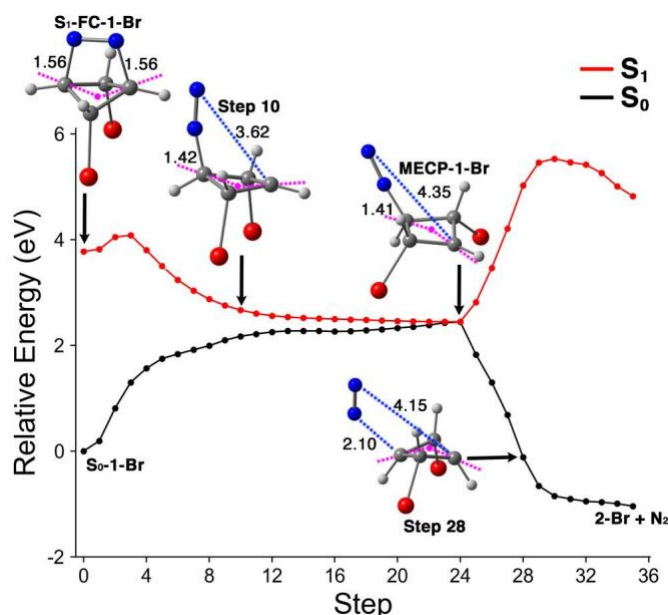


Figure 3. The minimum energy path from the **S₁-FC-1-Br** to **MECP-1-Br** and to **2-Br** with CASPT2(8,8)/ANO-S-VDZP//CASSCF(8,8)/ANO-S-VDZP. The blue dotted lines denote the C–N distance; the distances are in Angstrom. The pink dotted lines highlight the bicyclobutane dihedral angle θ . At step 10, $R_1 = 3.62\text{Å}$, $R_2 = 1.42\text{Å}$, $\theta = 159^\circ$, and $\alpha = -9^\circ$; at step 28, $R_1 = 4.15\text{Å}$, $R_2 = 2.10\text{Å}$, $\theta = 216^\circ$, and $\alpha = -20^\circ$.

The MEP in Figure 3 shows that the mechanism involves a stepwise breaking of the C–N bonds. The MEP suggests that there may be an S_1 -barrier (steps 1–4), this ‘local maximum’ may be an artifact resulting from the CASPT2(8,8)/ANO-S-VDZP single point energy calculations. The CASSCF(8,8)/ANO-S-VDZP MEP decreased smoothly (Figure S4). The S_1/S_0 ΔE decreases along the MEP and is < 0.50 eV at step 10, where one of the C–N bond has completely broken ($R_1 = 3.62\text{Å}$). Beyond this point, the MEP energies are nearly constant until the S_1/S_0 degeneracy region. We optimized a minimum energy crossing point based on the geometry at step 24 and located **MECP-1-Br**. The geometry of **MECP-1-Br** clearly shows inversion; the θ angle is 197° (Figure 2). From **MECP-1-Br**, the MEP calculation proceeded along the S_0 state. The subsequent path showed the second C–N bond breaking. Step 28 shows that the N–C distance R_2 was 2.10Å , while the bicyclobutane maintained the inverted dihedral angle, $\theta = 216^\circ$. We located **exo-2-Br** and an extruded N_2 at the end of MEP. Our MEP calculations have developed a static understanding of the photochemistry of **1-Br** and suggest that **exo-2-Br** is exclusively formed through a stepwise pathway.

Non-adiabatic molecular dynamics of 1. Experimental measurements of the photochemical reaction yield of diazabicyclo[2.1.1]hexenes (**1**) reveals an excess—but not exclusive—yield of bicyclo[1.1.0]butane with inverted stereochemistry. We turned to non-adiabatic molecular dynamics (NAMD) simulations to enumerate the possible photodynamics pathways and predict the yield of the competing stereoisomeric products. We have generated initial conditions for **1** with Wigner sampling at 300 K to create a broad region of Franck-Condon points and associated velocities. The initial geometries have sampled the C–N distances to range from 1.33 to 1.68Å , the bicyclobutane dihedral angle $\theta = 115$ – 138° , and the hydrogen dihedral angle $\alpha = -(8$ – $32)^\circ$.

Our NAMD results for **1** are based on 692 trajectories, for which 395 (57%) trajectories land on the ground-state with stepwise breaking of the C–N bonds, consistent with the static MEP findings. The other 297 (43%) trajectories remain in the S_1 -state at the end of 300 fs; we consider these trajectories to correspond to unfinished reactions. We identify three pathways post- S_1/S_0 intersections: the reversal to reactant **1**, the double-inversion product **exo-2**, and the retention product **endo-2**. Our simulations show a major product **exo-2** (71%), minor products **endo-2** (26%) and the reactant, **1** (3%). The predicted diastereomeric excesses of **exo-2** (46%) is in excellent agreement with the experiments (47%¹⁶). Emboldened by this excellent agreement with experiment, we sought to understand the bonding changes along the ground- and excited-state reaction pathways to reveal the origin of the stereoselectivity of **1**. We first plotted the trace of productive trajectories with respect to the distance of the first breaking C–N bond, R1 and the bicyclobutane dihedral angle θ in Figure 4a. The subplots in Figure 4b–4e highlights individual types of pathways during the second N–C bond breaking.

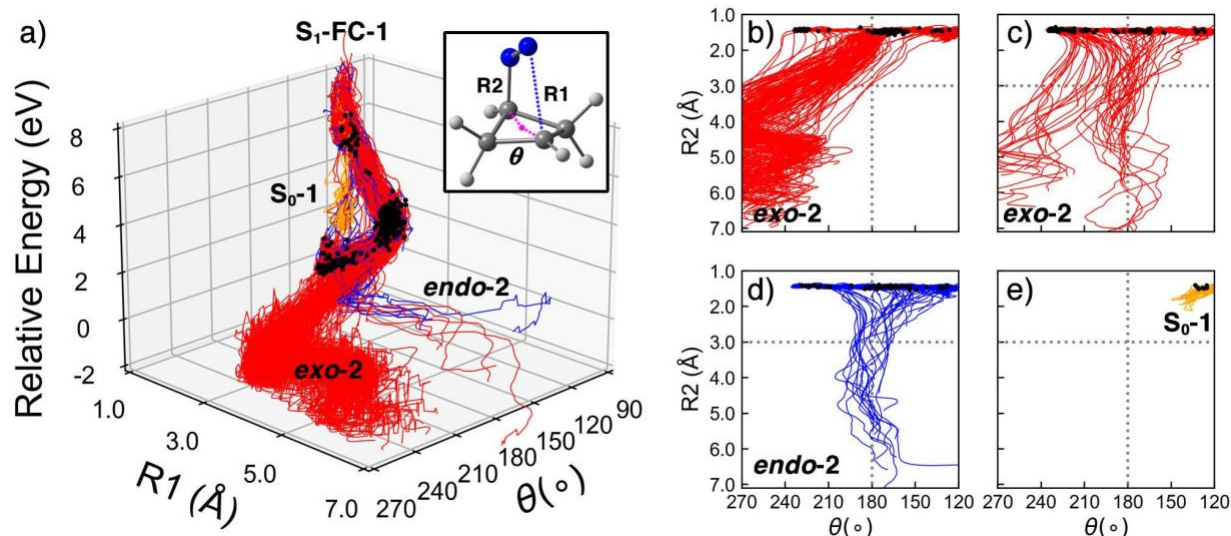


Figure 4. (a) The trajectories of **1** in 300 fs NAMD simulation with CASSCF(8,8)/ANO-S-VDZP. The plot monitors the N–C bond breaking and bicyclobutane inversion with R1 and θ . (b) The subplot of trajectories undergoing concerted N–C bond breaking and bicyclobutane inversion to **exo-2**. (c) The subplot of trajectories undergoing stepwise N–C bond breaking and bicyclobutane inversion to **exo-2**. (d) The subplot of trajectories undergoing stepwise N–C bond breaking and bicyclobutane retention to **endo-2**. (e) The subplot of trajectories reverted to **S₀-1**. The subplots (b)–(e) track the second C–N bond breaking and the inversion of bicyclobutane with R2 and θ . The black dots represent the latest surface hopping points.

The molecular trajectories rapidly moved away from the FC-region and approach hopping points (Figure 4a). The trajectories switched the electronic state to the ground-state via surface hopping points near/at the S_1/S_0 degeneracy region. 8% of the trajectories had ‘early’ hopping points with a single partially broken N–C bond has not been fully broken ($R1 = 1.49\text{--}2.16\text{Å}$ and $\theta = 125\text{--}139^\circ$). We identified a broad S_1/S_0 seam in the other trajectories ($R1 = 2.95\text{--}4.77\text{Å}$ and $\theta = 142\text{--}235^\circ$) (Figure 4a). We found 60% trajectories retained the bicyclobutane dihedral angle ($\theta < 180^\circ$) at the S_1/S_0 seam. However, tracking the dihedral angle, θ showed subsequent conversion from **endo-2** to **exo-2** in 42% trajectories. On the other hand, 32% trajectories have

shown double inversion ($\theta > 180^\circ$) at the S_1/S_0 seam, but 6% of the trajectories reverted from **exo-2** to **endo-2** in the end. The interconversion between **exo-2** and **endo-2** trajectories after the surface hopping points suggests the S_1/S_0 intersection does not fully control the stereoselectivity.

After the S_1/S_0 crossing, the trajectories of **1** (Figure 4b–4e) show that the second C–N bond continues to lengthen. We classified two ground-state mechanisms in these trajectories: 1) the second N–C bond breaking and the bicyclobutane inversion are occurring simultaneously (concerted mechanism), 2) the second C–N bond breaking and the bicyclobutane inversion are occurring stepwisely. All of the trajectories corresponding to the concerted mechanism are stereoselective to form **exo-2** (48% trajectories, Figure 4b). The stepwise mechanism extrudes N_2 before inverting (*i.e.*, θ). The resulting bicyclobutane molecule with $\theta > 210^\circ$ then retained the dihedral angle θ , which favors **exo-2** (Figure 4c). The trajectories with $\theta < 210^\circ$ vibrate about $\theta = 180^\circ$ (Figure 4c and Figure 4d). The stepwise mechanism results in an overall ratio of 0.9 : 1 between **exo-2** and **endo-2** (23% and 26% of the productive trajectories, respectively). Figure 4e characterizes the trajectories returned to **1**. It showed these trajectories were from the early S_1/S_0 crossing region; they revert to **1** because the C–N bonds are partially broken.

The trajectories show that the denitrogenation reaction begins in the S_1 -state and completes on the S_0 -state through a concerted or stepwise mechanistic pathway. To understand the ground-state topology of **1** and the stereoselectivity of the reaction, we computed the 2D PES of the ground states of **1**. Figure 5a and 5b show the 2D PES scanned with the bicyclobutane dihedral angle θ the hydrogen dihedral angle α of **1**.

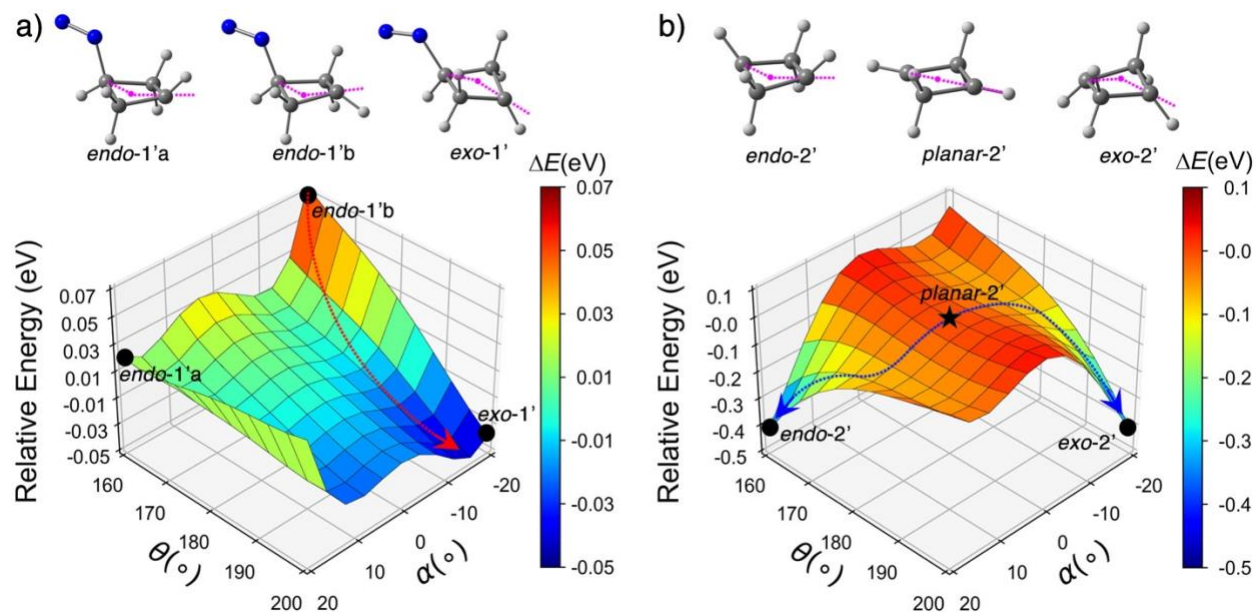


Figure 5. (a) The 2D PES of **1** with CASSCF(8,8)/ANO-S-VDZP. The red dotted arrow shows the deepest descent toward inverted bicyclobutane. (b) The 2D PES of **2** with CASSCF(2,2)/ANO-S-VDZP. The blue dotted arrows represent the symmetrically bifurcated relaxation paths to the retention and inversion structure. The star in (b) was confirmed as a second-order saddle point with CASSCF(2,2)/ANO-S-VDZP. The first imaginary mode corresponds to concerted vibrating of α , whereas the second imaginary mode represents stepwise alternating of α , which cannot be seen in (b). The geometries at black dots (star) are shown above the 2D PES.

Figure 5a is a ground-state PES for the concerted mechanism and the black dots correspond to the hopping points based on the trajectories in Figure 4b ($\theta = 126\text{--}234^\circ$ and $\alpha = -32\text{--}24^\circ$). There is a steep pathway (indicated with a red arrow) from $\theta = 160^\circ$ to 180° and from $\alpha = -20^\circ$ to -16° that is consistent with preferred conversion of **endo-2** to **exo-2** in the NAMD results discussed above. It also corroborates the previous interpretation of the stereoselectivity induced by impulsive population of the double-inversion vibrations.²² Figure 5b omits N_2 and uses the ground-state PES of **2** to approximate the PES for the stepwise mechanism. We assume that the trajectories start near the center of the 2D PES ($\theta = 180^\circ$ and $\alpha = 0^\circ$) because most of the trajectories vibrate around $\theta = 180^\circ$ in Figure 4c and 4d. The relaxation pathways bifurcate toward the local minima at $\theta = 160^\circ$; $\alpha = 20^\circ$ and $\theta = 200^\circ$; $\alpha = -20^\circ$, which resemble **endo-2** and **exo-2**, respectively. The symmetric pathways are consistent with the nearly equal **endo-2** and **exo-2** product ratio.

Non-adiabatic molecular dynamics of 1-Br. We extended our analysis of the reactivity, mechanism, and stereoselectivity beyond **1** to explore the excited-state landscape of halogenated diazabicyclo[2.1.1]hexenes (**1-Br**). We chose **1-Br** because it is the experimental precursor to **1-F** and **1-Cl**, which can be accessed with a thermal substitution reaction. As such, we performed NAMD simulations of **1-Br** to study the halogenation effects on the stereochemistry of **1** and **2**. Under identical computational conditions, 525 trajectories **1-Br** trajectories landed on the ground-state (out of 596) showing a reaction “yield” of 88%. This is considerably larger than that of the parent **1**. The increasing photolysis efficiency of **1-Br** could compensate for the weakened absorption ability predicted by the oscillator strengths (Table 1). Our trajectory statistics demonstrate that 97% trajectories formed **exo-2-Br**, whereas 3% formed **endo-2-Br**, which corresponds to a predicted diastereomeric excess of 94% for **exo-2-Br**. We also observed a single trajectory that reverts to **S₀-1-Br** (0.2%). The trajectories from **S₁-FC-1-Br** are plotted with respect to distance of the first breaking C–N bond, R1 and the bicyclobutane dihedral angle θ in Figure 6a. The subplots in Figure 6b–6d highlights the concerted, the stepwise, and the reverted mechanism during the second C–N bond breaking of **1-Br**.

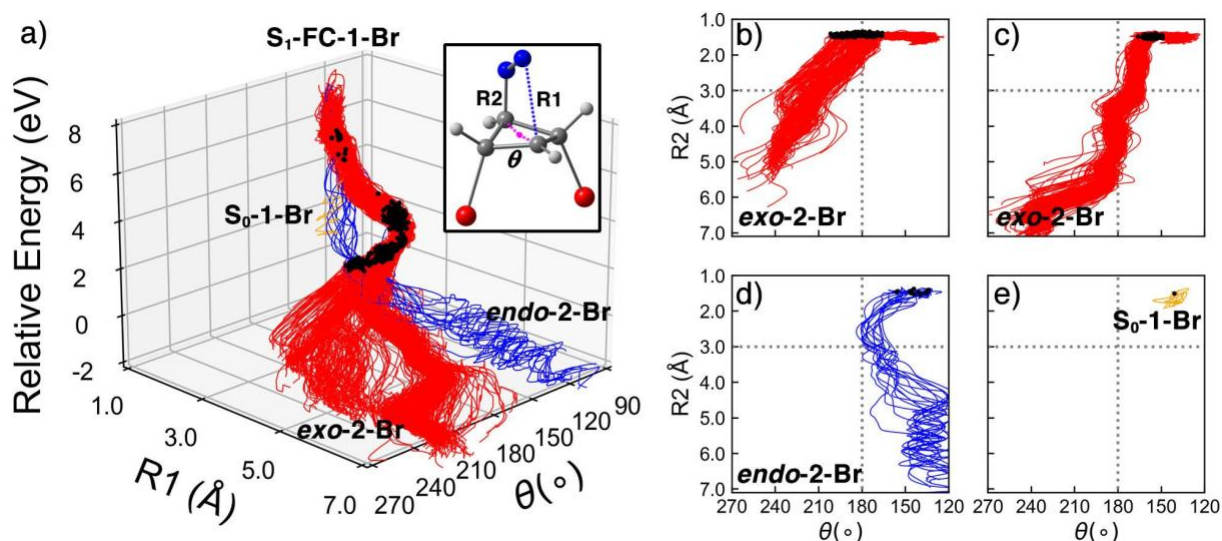


Figure 6. (a) The trajectories of **1-Br** in 300 fs NAMD simulation with CASSCF(8,8)/ ANO-S-VDZP. The plot monitors the N–C bond breaking and bicyclobutane inversion with R1 and θ . (b) The subplot of trajectories undergoing concerted N–C bond breaking and bicyclobutane inversion to **exo-2-Br**. (c) The subplot of trajectories undergoing stepwise N–C bond breaking and bicyclobutane inversion to **exo-2-Br**. (d) The subplot of trajectories undergoing stepwise N–C bond breaking and bicyclobutane retention to **endo-2-Br**. (e) The subplot of trajectories reverted to **1-Br**. The subplots (b)–(e) track the second C–N bond breaking and the inversion of bicyclobutane with R2 and θ .

The denitrogenation of **1-Br**—like the parent—begins in the excited-state and completes in the ground state. The trajectories reached **exo-2-Br** via a S_1/S_0 crossing seam at $R1 = 3.50\text{--}4.63 \text{ \AA}$ and $\theta = 149\text{--}202^\circ$. At the S_1/S_0 seam, 28% trajectories inverted the bicyclobutane ($\theta > 180^\circ$) and maintained the angle in **exo-2-Br**. 71% trajectories retain the bicyclobutane dihedral angle θ ($\theta < 180^\circ$), but only 2% trajectories conserved θ to form **endo-2-Br** when they hopped to the ground-state. Another 1% of the trajectories passed a S_1/S_0 crossing region at $R1 = 1.67\text{--}2.35 \text{ \AA}$ and $\theta = 134\text{--}148^\circ$ toward **endo-2-Br**. Figure 6b shows the concerted second C–N bond breaking and bicyclobutane inversion towards **exo-2-Br** (43% trajectories). Figure 6c and 6d shows the stepwise mechanism where N_2 is extruded before the bicyclobutane inverts. In contrast to the nearly 1: 1 ratio in the parent, the **1-Br** trajectories undergoing stepwise mechanism significantly prefer **exo-2-Br** (54% trajectories) over **endo-2-Br** (3% trajectories). Figure 6e illustrates the single trajectory that reverts to S_0 -**1-Br**.

We again computed the 2D PESs of **1-Br** to understand the topologies and rationalize the mechanism and predicted stereoselectivity of **1-Br**. The PESs scanned along the bicyclobutane dihedral angle θ and the hydrogen dihedral angle α , which are shown in Figure 7a and 7b.

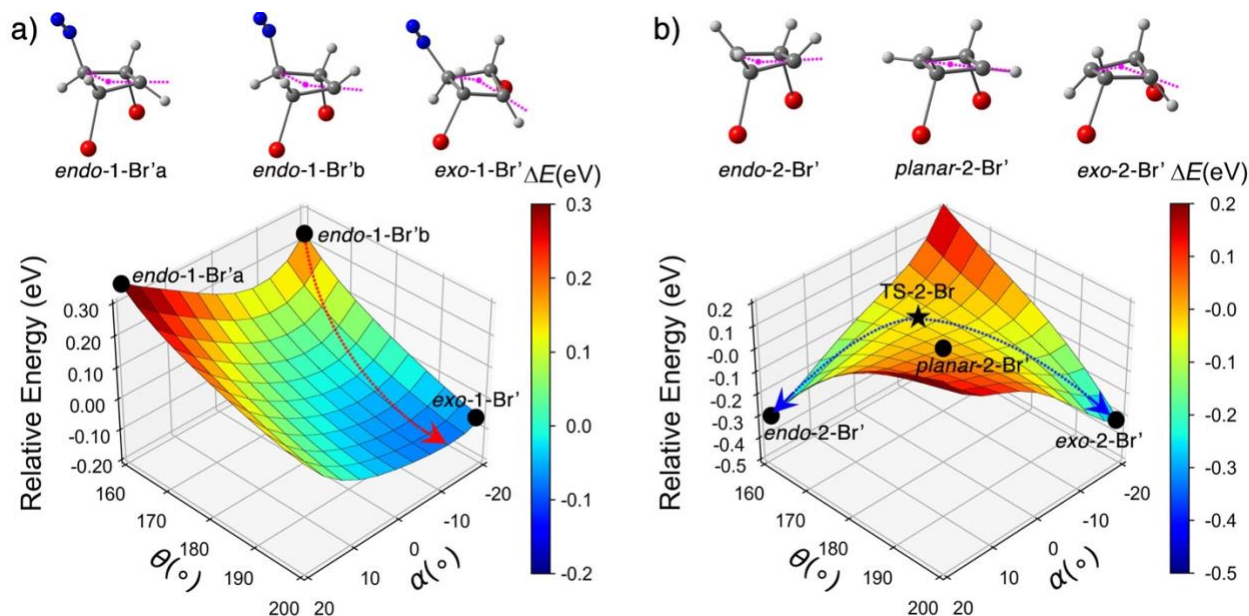


Figure 7. (a) The 2D PES of **1-Br** with CASSCF(8,8)/ANO-S-VDZP, where the N–C distance was constrained at 1.48 \AA . The red dotted arrow shows a path favoring the inversion of bicyclobutane. (b) The 2D PES of **2-Br** with CASSCF(2,2)/ANO-S-VDZP. The blue dotted arrows represent the

asymmetrically bifurcated relaxation paths, which is more inclined toward inversion structure. The star in (b) was confirmed as a transition state with CASSCF(2,2)/ANO-S-VDZP. The geometries at black dots are shown above the 2D PES.

The 2D PES scan of **1-Br** in Figure 7a surveys the concerted mechanism; the second C–N bond is constrained at 1.48 Å to prevent N₂ from extruding at some geometries. We marked the hopping points in Figure 7a that correspond to the S₁/S₀ seam geometries ($\theta=149\text{--}202^\circ$, Figure 6a). The PES shows a local minimum at $\theta = 200^\circ$ and $\alpha = -12^\circ$ that resembles an inverted bicyclobutane. This suggests that **1-Br** is stereoselective for **exo-2-Br** with the concerted mechanism, which is consistent with the stereoselectivity of the parent. Figure 7b shows the PES for the stepwise mechanism, where the N₂ has already dissociated. The PES of **1-Br** is quite different from the corresponding PES in Figure 5b. The PES for **1-Br** is not symmetric like that of **1**; the transition structure connecting **exo-2** and **endo-2** is in the center of the PES. The transition structure connecting **exo-2-Br** and **endo-2-Br** (**TS-2-Br**) is skewed towards the disfavored product, **endo-2-Br**. We hypothesized that the unsymmetric PES disproportionately lowered the energies of *exo*-like geometries. It arose from a hyperconjugative interaction between the carbon lone pair orbital and the $\sigma^*_{\text{C-Br}}$ -orbital. For example, the C–Br distance in **TS-2-Br** is 2.00 Å, which is 0.08 Å longer than the that in **1-Br** (1.92 Å). This increase in the $\sigma_{\text{C-Br}}$ bond length and the antiperiplanar relationship between the lone pair (n_{C}) and the $\sigma^*_{\text{C-Br}}$ orbitals suggests that a favorable $n_{\text{C}} \rightarrow \sigma^*_{\text{C-Br}}$ hyperconjugation is occurring. Figure 8 illustrates the NBOs participating in **TS-2-Br** and **planar-2-Br'** along with their second-order perturbation interaction energy, $E^{(2)}$.

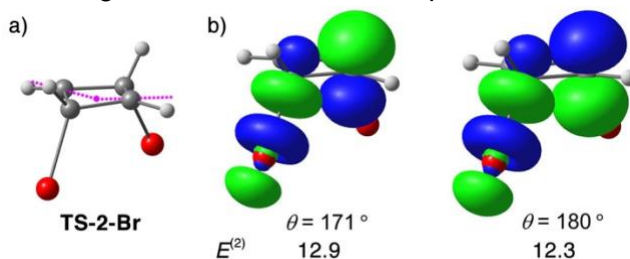


Figure 8. (a) The optimized geometry of **TS-2-Br** with CASSCF(2,2)/ANO-S-VDZP. $\theta = 171^\circ$ and $\alpha = -6^\circ$. (b) Hyperconjugation of $n_{\text{C}} \rightarrow \sigma^*_{\text{C-Br}}$ in terms of natural bond orbital interactions in **TS-2-Br** (left) and the planar **2-Br'** (right). The $E^{(2)}$ energies are in kcal mol⁻¹.

At the PES center in Figure 7b, **planar-2-Br'** is 0.7 kcal mol⁻¹ higher than **TS-2-Br** (Figure 7b). The $E^{(2)}$ of **TS-2-Br** is 0.6 kcal mol⁻¹ larger than that of **planar-2-Br'**, which suggests the bicyclobutane dihedral angle $\theta = 171^\circ$ can lower the transition state energy with $n_{\text{C}} \rightarrow \sigma^*_{\text{C-Br}}$ hyperconjugative interactions. Consequently, the transition structure changes its relative position from the center of the PES (**planar-2-Br'**) toward **endo-2-Br** thus resulting in larger shoulder region for relaxation to **exo-2-Br**. Based on Figure 6c and 6d, we can assume the trajectories post S₁/S₀ surface hopping start at $\theta = 160\text{--}200^\circ$, thus most of them (54% vs. 3%) land on the downhill path towards **exo-2-Br**.

Non-adiabatic molecular dynamics of 1-F and 1-Cl. We continued our studies to two theoretical diazabicyclo[2.1.1]hexenes, **1-F** and **1-Cl**. We performed 672 and 568 NAMD trajectories to test our developing stereochemistry model. The simulations predicted 87% “yield” in **1-F** and **1-Cl**, which are similar to **1-Br** (88%). The major products of **1-F** and **1-Cl** preferred double inversion

(**exo-2-F**: 98% vs. **endo-2-F**: 1% and **exo-2-Cl**: 98% vs. **endo-2-Cl**: 2%). Our trajectories predicted a diastereomeric excess of 97% and 96%, respectively. The trajectory characterization (Figure S5 and Figure S6) confirmed the coexistence of concerted and stepwise N₂ extrusion mechanisms in **1-F** and **1-Cl**. The PES calculations for fluorinated and chlorinated derivatives (Figure S7 and Figure S8) illustrated that the concerted mechanism also favors double inversion. In the stepwise mechanism, we observe a similar broad path to the corresponding inverted products, thus enhancing the stereoselectivities. We located transition structures analogous to **TS-2-Br**, **TS-2-F** and **TS-2-Cl**, which show a similar structural pyramidalization [**TS-2-F**: $\theta = 174^\circ$; **TS-2-Cl**: $\theta = 169^\circ$]. We interpret this as a necessary structural change to benefit from the $n_C \rightarrow \sigma^*_{C-F,Cl}$ hyperconjugative interaction (Figure S9). Therefore, the post-surface hopping trajectories of **1-F** and **1-Cl** with $\theta = 180 \pm 10^\circ$ favor the steeper path to double inversion.

Concluding Remarks

Our NAMD simulation shows a consistent halogenation effect that remarkably enhances the stereoselectivity in the photochemical denitrogenation of **1** producing nearly exclusive double inversion products. We have used complete active space self-consistent field (CASSCF) calculations with an (8,8) active space and ANO-S-VDZP basis set to study the photophysics and photochemistries of **1**, **1-F**, **1-Cl**, and **1-Br**. Our calculations and NAMD simulations predict that photochemistry of **1-F**, **1-Cl**, and **1-Br** will be efficient and favor double inversion pathways and products.

The CASPT2(8,8)/ANO-S-VDZP//CASSCF(8,8)/ANO-S-VDZP calculations presented here suggest that **1**, **1-F**, **1-Cl**, and **1-Br** will feature $n \rightarrow \pi^*$ transitions with excitation energies ranging from 3.77 to 3.91 eV. The minimum energy path calculation of **1-Br** showed stepwise C–N bond breaking and characterized a minimum energy crossing point that favors double inversion. We computed 692 non-adiabatic molecular dynamics trajectories of **1** and identified competing stereoselective and non-stereoselective paths. 48% trajectories followed the stereoselective paths, where the N₂ extrusion and bicyclobutane inversion were occurring simultaneously. The non-stereoselective paths extruded N₂ with a nearly planar bicyclobutane; 23% and 26% of the trajectories led to **exo-2** and **endo-2**, respectively. The total trajectories undergoing the two mechanisms successfully reproduced the stereoselective double inversion of **2** (calc.d.e. = 46% vs. exp.d.e. = 47%).

We have showed that halogenation plays a substantial role controlling the stereochemistry in the photochemical denitrogenation of **1**. We predict a considerably higher stereoselectivity of double inversion than **1** with 94% diastereomeric excess of **exo-2-Br**. The enhancement of stereoselectivity results from stepwise N₂ extrusion mechanism, in which 54% trajectories favored the **exo-2-Br** and 3% trajectories lead to **endo-2-Br**. The static PES calculations showed **TS-2-Br** was skewed toward **endo-2-Br** resulting broader relaxation region to **exo-2-Br**. Consequently, most of post-surface hopping trajectories in stepwise mechanism with nearly planar **2-Br** ($\theta = 180 \pm 10^\circ$) favor the downhill path to **exo-2-Br**. Our calculation revealed that the **TS-2-Br** is 0.7 kcal mol⁻¹ lower energy than that of **planar-2-Br'**, stabilized by the hyperconjugative ($n_C \rightarrow \sigma^*_{C-Br}$) interactions. We have found consistent conclusions in **1-F** and **1-Cl**, which demonstrates the essential role of $n_C \rightarrow \sigma^*_{C-X}$, X = F, Cl, Br hyperconjugation on the increased stereoselectivity for halogenated diazabicyclo[2.1.1]hexenes.

Supporting Information

Excitation energies. Active spaces, optimized geometries, and minimum energy paths for **1**, **1-F** and **1-Cl**. NAMD trajectories and 2D PES for **1-F** and **1-Cl**. Hyperconjugation in **2-F** and **2-Cl**. Cartesian coordinates for optimized geometries.

Acknowledgments

J.L. and S.A.L. acknowledges Dr. Jordan. M. Cox for helpful discussion on the NAMD trajectories. S.A.L. acknowledge the Office of Naval Research (ONR N00014-12-1-0828) and the National Science Foundation (NSF-1940307) for funding this research. J.L. R.S. and S.A.L. appreciate the assistance from the Northeastern Research Computing Team and access to the computing resources of the Discovery cluster.

References

1. Horvath, I. T.; Anastas, P. T., Innovations and green chemistry. *Chem. Rev.* **2007**, *107* (6), 2169-2173.
2. Khoury, P. R.; Goddard, J. D.; Tam, W., Ring strain energies: substituted rings, norbornanes, norbornenes and norbornadienes. *Tetrahedron* **2004**, *60* (37), 8103-8112.
3. Fawcett, A.; Biberger, T.; Aggarwal, V. K., Carbopalladation of C-C sigma-bonds enabled by strained boronate complexes. *Nat Chem* **2019**, *11* (2), 117-122.
4. Gianatassio, R.; Lopchuk, J. M.; Wang, J.; Pan, C. M.; Malins, L. R.; Prieto, L.; Brandt, T. A.; Collins, M. R.; Gallego, G. M.; Sach, N. W.; Spangler, J. E.; Zhu, H.; Zhu, J.; Baran, P. S., Organic chemistry. Strain-release amination. *Science* **2016**, *351* (6270), 241-246.
5. Chen, K.; Huang, X.; Kan, S. B. J.; Zhang, R. K.; Arnold, F. H., Enzymatic construction of highly strained carbocycles. *Science* **2018**, *360* (6384), 71-75.
6. Fawcett, A., Recent advances in the chemistry of bicyclo- and 1-azabicyclo[1.1.0]butanes. *Pure Appl. Chem.* **2020**, *92* (5), 751-765.
7. Walczak, M. A.; Krainz, T.; Wipf, P., Ring-strain-enabled reaction discovery: new heterocycles from bicyclo[1.1.0]butanes. *Acc. Chem. Res.* **2015**, *48* (4), 1149-1158.
8. Chang, M. H.; Dougherty, D. A., 2,3-Diazabicyclo[2.1.1]hex-2-ene. Synthesis and thermal decomposition. *The Journal of Organic Chemistry* **1981**, *46* (20), 4092-4093.
9. Gaoni, Y., Preparation of ring-substituted (arylsulfonyl)cyclopropanes and (arylsulfonyl)bicyclobutanes from .gamma.,.delta.-epoxy sulfones. *The Journal of Organic Chemistry* **1982**, *47* (13), 2564-2571.
10. Panish, R.; Chintala, S. R.; Boruta, D. T.; Fang, Y.; Taylor, M. T.; Fox, J. M., Enantioselective synthesis of cyclobutanes via sequential Rh-catalyzed bicyclobutanation/Cu-catalyzed homoconjugate addition. *J. Am. Chem. Soc.* **2013**, *135* (25), 9283-9286.
11. Tokunaga, K.; Sato, M.; Kuwata, K.; Miura, C.; Fuchida, H.; Matsunaga, N.; Koyanagi, S.; Ohdo, S.; Shindo, N.; Ojida, A., Bicyclobutane Carboxylic Amide as a Cysteine-Directed Strained Electrophile for Selective Targeting of Proteins. *J. Am. Chem. Soc.* **2020**, *142* (43), 18522-18531.
12. Wipf, P.; Stephenson, C. R.; Okumura, K., Transition-metal-mediated cascade reactions: C,C-dicyclopropylmethylamines by way of double C,C-sigma-bond insertion into bicyclobutanes. *J. Am. Chem. Soc.* **2003**, *125* (48), 14694-14695.
13. Chang, M. H.; Dougherty, D. A., Phase-dependent stereochemistry and chemical activation in the thermal decomposition of 2,3-diazabicyclo[2.1.1]hexene. *J. Am. Chem. Soc.* **1982**, *104* (4), 1131-1132.
14. Chang, M. H.; Jain, R.; Dougherty, D. A., Chemical activation as a probe of reaction mechanism. Synthesis and thermal decomposition of 2,3-diazabicyclo[2.1.1]hex-2-enes. *J. Am. Chem. Soc.* **1984**, *106* (15), 4211-4217.

15. Peterson, T. H.; Carpenter, B. K., Estimation of dynamic effects on product ratios by vectorial decomposition of a reaction coordinate. Application to thermal nitrogen loss from bicyclic azo compounds. *J. Am. Chem. Soc.* **1992**, *114* (2), 766-767.
16. Chang, M. H.; Dougherty, D. A., Photochemistry of 2,3-diazabicyclo[2.1.1]hex-2-ene. .beta. Carbon-carbon cleavage to a stereorandom triplet biradical. *J. Am. Chem. Soc.* **1982**, *104* (8), 2333-2334.
17. Adam, W.; García, H.; Martí, V.; Moorthy, J. N.; Peters, K.; Peters, E.-M., Photochemical Denitrogenation of Norbornene-Annelated 2,3-Diazabicyclo[2.1.1]hept-2-ene-Type Azoalkanes: Crystal-Lattice versus Zeolite-Interior Effects. *J. Am. Chem. Soc.* **2000**, *122* (14), 3536-3537.
18. Roth, W. R.; Martin, M., Zur Stereochemie des thermischen und photochemischen Zerfalls von 2.3-Diaza-bicyclo[2.2.1]hepten-(2). *Justus Liebigs Annalen der Chemie* **1967**, *702* (1), 1-7.
19. Adam, W.; Diederling, M.; Trofimov, A. V., Intriguing double-inversion stereochemistry in the denitrogenation of 2,3-diazabicyclo[2.2.1]heptene-type azoalkanes: a model mechanistic study in physical organic chemistry. *J. Phys. Org. Chem.* **2004**, *17* (8), 643-655.
20. Adam, W.; Denninger, U.; Finzel, R.; Kita, F.; Platsch, H.; Walter, H.; Zang, G., Comparative study of the pyrolysis, photoinduced electron transfer (PET), and laser-jet and 185-nm photochemistry of alkyl-substituted bicyclic azoalkanes. *J. Am. Chem. Soc.* **1992**, *114* (13), 5027-5035.
21. Yamamoto, N.; Olivucci, M.; Celani, P.; Bernardi, F.; Robb, M. A., An MC-SCF/MP2 Study of the Photochemistry of 2,3-Diazabicyclo[2.2.1]hept-2-ene: Production and Fate of Diazenyl and Hydrazonyl Biradicals. *J. Am. Chem. Soc.* **1998**, *120* (10), 2391-2407.
22. Sinicropi, A.; Page, C. S.; Adam, W.; Olivucci, M., Computational study on the origin of the stereoselectivity for the photochemical denitrogenation of diazabicycloheptene. *J. Am. Chem. Soc.* **2003**, *125* (36), 10947-10959.
23. Chen, H.; Li, S., CASPT2//CASSCF study on the photolysis mechanism of 2,3-diazabicyclo[2.1.1]hex-2-ene: alpha C-N versus beta C-C cleavage. *J. Org. Chem.* **2006**, *71* (24), 9013-9022.
24. Abe, M.; Hatano, S., Mechanistic study of stereoselectivity in azoalkane denitrogenations. *Pure Appl. Chem.* **2017**, *89* (6), 759-764.
25. Fdez Galvan, I.; Vacher, M.; Alavi, A.; Angeli, C.; Aquilante, F.; Autschbach, J.; Bao, J. J.; Bokarev, S. I.; Bogdanov, N. A.; Carlson, R. K.; Chibotaru, L. F.; Creutzberg, J.; Dattani, N.; Delcey, M. G.; Dong, S. S.; Dreuw, A.; Freitag, L.; Frutos, L. M.; Gagliardi, L.; Gendron, F.; Giussani, A.; Gonzalez, L.; Grell, G.; Guo, M.; Hoyer, C. E.; Johansson, M.; Keller, S.; Knecht, S.; Kovacevic, G.; Kallman, E.; Li Manni, G.; Lundberg, M.; Ma, Y.; Mai, S.; Malhado, J. P.; Malmqvist, P. A.; Marquetand, P.; Mewes, S. A.; Norell, J.; Olivucci, M.; Oppel, M.; Phung, Q. M.; Pierloot, K.; Plasser, F.; Reiher, M.; Sand, A. M.; Schapiro, I.; Sharma, P.; Stein, C. J.; Sorensen, L. K.; Truhlar, D. G.; Ugandi, M.; Ungur, L.; Valentini, A.; Vancoillie, S.; Veryazov, V.; Weser, O.; Wesolowski, T. A.; Widmark, P. O.; Wouters, S.; Zech, A.; Zobel, J. P.; Lindh, R., OpenMolcas: From Source Code to Insight. *J. Chem. Theory Comput.* **2019**, *15* (11), 5925-5964.
26. Jacquemin, D.; Perpète, E. A.; Ciofini, I.; Adamo, C., On the TD-DFT UV/vis spectra accuracy: the azoalkanes. *Theor. Chem. Acc.* **2008**, *120* (4-6), 405-410.
27. Pierloot, K.; Dumez, B.; Widmark, P.-O.; Roos, B. r. O., Density matrix averaged atomic natural orbital (ANO) basis sets for correlated molecular wave functions. *Theor. Chim. Acta* **1995**, *90* (2-3), 87-114.
28. Pou-Amérigo, R.; Merchán, M.; Nebot-Gil, I.; Widmark, P.-O.; Roos, B. O., Density matrix averaged atomic natural orbital (ANO) basis sets for correlated molecular wave functions. *Theor. Chim. Acta* **1995**, *92* (3), 149-181.
29. Widmark, P.-O.; Malmqvist, P.-k.; Roos, B. r. O., Density matrix averaged atomic natural orbital (ANO) basis sets for correlated molecular wave functions. *Theor. Chim. Acta* **1990**, *77* (5), 291-306.

30. Widmark, P.-O.; Persson, B. J.; Roos, B. r. O., Density matrix averaged atomic natural orbital (ANO) basis sets for correlated molecular wave functions. *Theor. Chim. Acta* **1991**, 79 (6), 419-432.
31. Roos, B. O.; Andersson, K., Multiconfigurational perturbation theory with level shift — the Cr2 potential revisited. *Chem. Phys. Lett.* **1995**, 245 (2-3), 215-223.
32. Roos, B. O.; Andersson, K.; Fülcher, M. P.; Serrano-Andrés, L.; Pierloot, K.; Merchán, M.; Molina, V., Applications of level shift corrected perturbation theory in electronic spectroscopy. *J. MOL. STRUC-THEOCHEM* **1996**, 388, 257-276.
33. Martyna, G. J.; Tuckerman, M. E.; Tobias, D. J.; Klein, M. L., Explicit reversible integrators for extended systems dynamics. *Mol. Phys.* **1996**, 87 (5), 1117-1157.
34. Hammes - Schiffer, S.; Tully, J. C., Proton transfer in solution: Molecular dynamics with quantum transitions. *J. Chem. Phys.* **1994**, 101 (6), 4657-4667.
35. Tully, J. C., Molecular dynamics with electronic transitions. *J. Chem. Phys.* **1990**, 93 (2), 1061-1071.
36. Tully, J. C.; Preston, R. K., Trajectory Surface Hopping Approach to Nonadiabatic Molecular Collisions: The Reaction of H+ with D2. *J. Chem. Phys.* **1971**, 55 (2), 562-572.
37. Reed, A. E.; Curtiss, L. A.; Weinhold, F., Intermolecular interactions from a natural bond orbital, donor-acceptor viewpoint. *Chem. Rev.* **1988**, 88 (6), 899-926.
38. E. D. Glendening, J. K. B., A. E. Reed, J. E. Carpenter, J. A. Bohmann, C. M. Morales, C. R. Landis, and F. Weinhold *NBO 6.0*, Theoretical Chemistry Institute, University of Wisconsin, Madison: 2013.
39. Perdew, J. P.; Burke, K.; Ernzerhof, M., Generalized Gradient Approximation Made Simple. *Phys. Rev. Lett.* **1996**, 77 (18), 3865-3868.
40. Perdew, J. P.; Burke, K.; Ernzerhof, M., Generalized Gradient Approximation Made Simple [Phys. Rev. Lett. 77, 3865 (1996)]. *Phys. Rev. Lett.* **1997**, 78 (7), 1396-1396.
41. Dunning, T. H., Gaussian basis sets for use in correlated molecular calculations. I. The atoms boron through neon and hydrogen. *J. Chem. Phys.* **1989**, 90 (2), 1007-1023.
42. Neese, F., The ORCA program system. *Wiley Interdiscip. Rev. Comput. Mol. Sci.* **2012**, 2 (1), 73-78.
43. Noodleman, L., Valence bond description of antiferromagnetic coupling in transition metal dimers. *J. Chem. Phys.* **1981**, 74 (10), 5737-5743.

TOC

